Composite Structures 357 (2025) 118889

Contents lists available at ScienceDirect

Composite Structures

journal homepage: www.elsevier.com/locate/compstruct

Experimental testing and micromechanical modelling of unidirectional CFRP composite laminae under multiaxial loading conditions☆

Lei Wan [a,b], Ka Zhang [a], Jiayun Chen [a,c], Aonan Li [a], Jiang Wu [a], Dongmin Yang [a,*]

[a] Institute for Materials and Processes, School of Engineering, University of Edinburgh, Edinburgh EH9 3FB, UK
[b] School of Engineering, University of Hull, Hull HU6 7RX, UK
[c] College of General Aviation and Flight, Nanjing University of Aeronautics and Astronautics, Nanjing 210016, China

ARTICLE INFO

Keywords:
Multiaxial loading
CFRPs
Finite element modelling
Failure strength
RVE

ABSTRACT

This paper presents comprehensive experimental testing and numerical modelling of the failure behaviours of unidirectional carbon fibre reinforced polymer (UD-CFRP) composite laminae under multiaxial loading conditions. A novel modified Arcan test rig with a rotational clamp was developed to enable multiple stress combinations with out-of-plane stresses in UD laminae on a traditional laboratory-based uniaxial test machine. The test rig was verified by uniaxial tension and validated by off-axis tension. UD CFRP laminae were tested for the first time under five stress combinations using the test rig, with results cross-validated against a high-fidelity representative volume element (RVE)-based 3D micromechanical finite element model. Failure strength envelope and damage mechanisms demonstrate the applicability of the test rig for composite failure under multiaxial loading conditions with a broad spectrum of stress combinations.

1. Introduction

Ever since the application of carbon fibre reinforced polymer (CFRP) composite laminates in the 1960s, their design and analysis have been evolving from simple Rule of Mixture (RoM) to empirical failure criteria, e.g., Tsai–Wu [1], Hashin [2], Puck [3] and Pinho [4]. Conservative design is usually adopted for composite laminates but inaccurate predictions of strength have presented a long-standing challenge. This is exaggerated and more ubiquitous in the presence of cyclic or impact loads. To address this challenge, QinetiQ has organised three World Wide Failure Exercises (WWFE-I, -II, -III), and the recently completed WWFE-II [5] has shown that none of the participating failure criteria could accurately predict the 13 selected static loading cases.

One of the main issues that hinders the improvement of failure criteria is the lack of sufficient experimental data (particularly from multiaxial tests), which makes benchmarking and validation of theoretical/numerical predictions very challenging. In addition to uniaxial loading conditions, some biaxial and triaxial loading conditions can be achieved with developed fixtures or facilities (see Fig. 1). Biaxial loading fixtures can be divided into two types, i.e., one combines axial and shear loadings, and the other provides two axial loadings [6–8]. Few of them can achieve decoupled loadings due to the limitations of the structural design [9,10]. The most common test method for achieving the triaxial loading condition is the off-axis test for the unidirectional (UD) laminae [11,12], but it can only realise in-plane cases and the two axial loadings are limited to the specific directions. Triaxial-normal stress conditions can also be realised, but large facilities are needed [13,14]. Especially, uncoupled triaxial loadings can be realised with the facility in Fig. 1(b.4).

As part of the initiative attempting to address these challenges, in this paper, a novel multiaxial test rig was conceptualised, designed, and prototyped to test the UD composite laminae in multiaxial loading scenarios in a stress space with up to five stresses. Verified by conventional uniaxial tensile tests and benchmarked against off-axis and biaxial tensile-shear loading tests, the test rig was adopted for multiaxial loading alongside high-fidelity RVE modelling and X-ray microtomography (μCT), for the first time demonstrating the potential of the integrated approach for composite failure prediction. A widely used CF/epoxy UD lamina (IM7/8552) provided by Hexcel was chosen for the benchmark tests. The material system is consistent with previous work in WWFEs and provides additional experimental data for validating the multiaxial rig and proposed model. The traditional off-axis tension testing technique was adopted to obtain the material response in $\sigma_{11}-\sigma_{22}-\sigma_{12}$ stress space (1 is the fibre direction). Biaxial tests are performed for the stress space of $\sigma_{11}-\sigma_{12}$. Another stress space $\sigma_{22}-\sigma_{21}$ could be achieved by loading on 90° ply specimens. The test data together with other experimental databases available

☆ All authors contribute equally.
* Corresponding author.
E-mail address: Dongmin.Yang@ed.ac.uk (D. Yang).

https://doi.org/10.1016/j.compstruct.2025.118889
Received 16 September 2024; Received in revised form 25 December 2024; Accepted 22 January 2025
Available online 5 February 2025

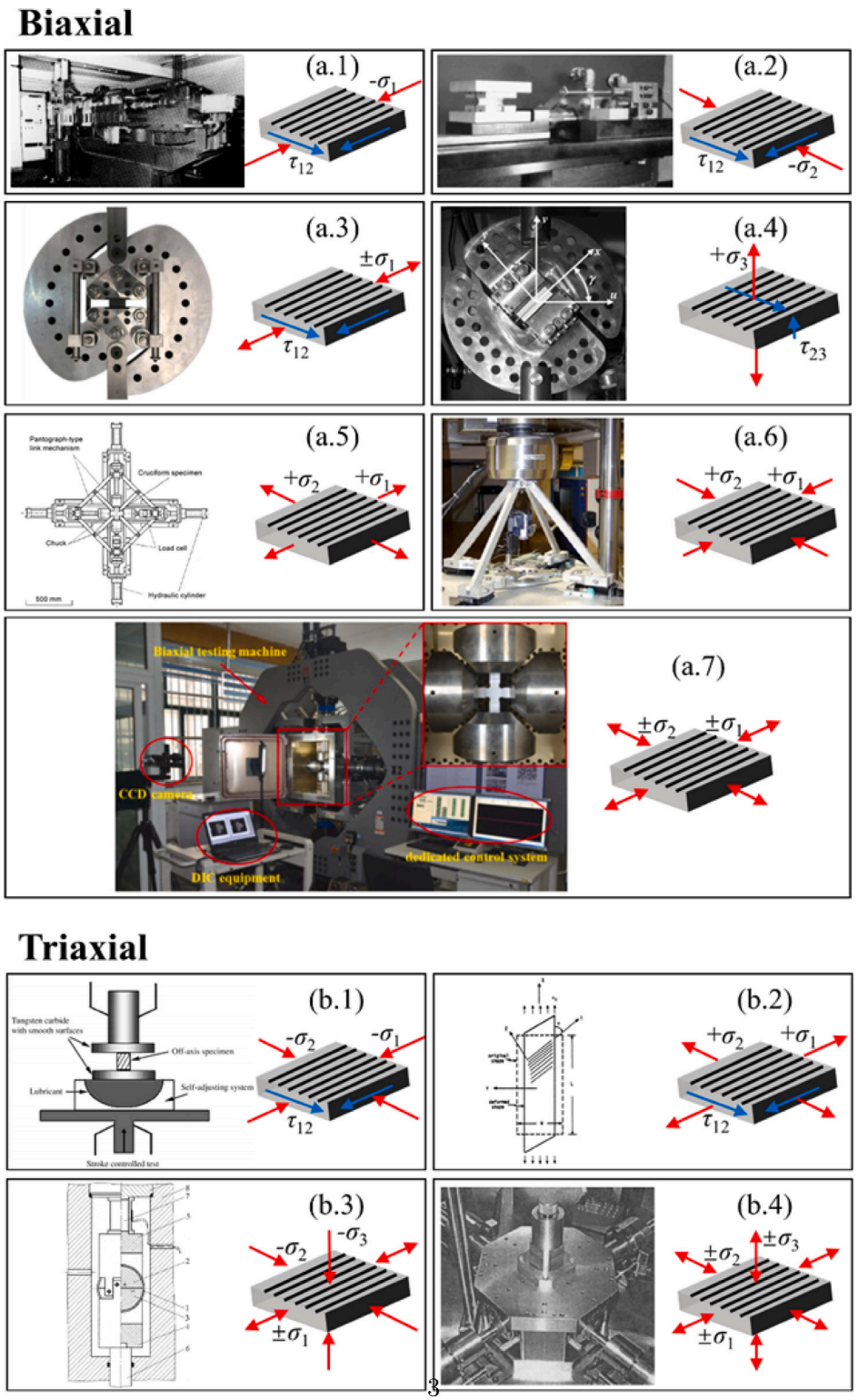

Fig. 1. (a) The fixtures provide biaxial loading conditions [6–10]; (b) The fixtures provide triaxial loading conditions [11–14].

for IM7/8552 are used to benchmark the multiaxial testing rig. With samples cut at different angles with respect to the fibre direction, the rig allows multiaxial loading tests of composite laminae/laminates, covering broader stress spaces of $\sigma_{11} - \sigma_{12} - \sigma_{13}$, $\sigma_{11} - \sigma_{12} - \sigma_{23}$, $\sigma_{33} - \sigma_{13} - \sigma_{23}$, $\sigma_{11} - \sigma_{12} - \sigma_{13} - \sigma_{22}$, $\sigma_{11} - \sigma_{22} - \sigma_{12} - \sigma_{13} - \sigma_{23}$.

The paper is organised with the following structure. In Section 2, the design of multiaxial rig is introduced, and the multiaxial loading tests for UD CFRP specimen are implemented. In Section 3, the microstructure, constitutive models and boundary conditions of the 3D micromechanical model are introduced. In Section 4, benchmarking of the multiaxial rig under off-axis and biaxial tension is conducted and the failure analysis of the UD CFRP laminae under multiaxial loadings based on experimental results and RVE modelling is discussed in Section 5. Finally, conclusions are drawn in Section 6.

2. Multiaxial rig development and experimental tests

2.1. Concept and design of multiaxial test rig

The modified Arcan multiaxial test rig consists of a pair of outer arms, a pair of interior arms, a pair of rotation clamps and four anti-buckling rails. The outer arms are connected with a standard test machine (such as Instron) with a hooker and pins. The inner arms are connected to the outer arms also with pins for easy disassembly and assembly, and the rotation clamps are connected to the interior arms with bolts. The specimen is secured in the centre of the fixture by mechanical grips to ensure a uniform clamping pressure applied to the specimen tabs.

Holes are created on the arms at an interval angle of 15° to allow a broad range of loading combinations. The holders for the anti-buckling rails are mounted on the outer arms, the positions of which are determined according to the loading angle so that it is always aligned with the uniaxial loading in Z-axis direction. Linear guide bearings are used to allow the sliding of each rail, with one end locked by a clutch and the other end set free.

By rotating the arms with respect to the anti-buckling rails and the rotation clamps, a specific angle can be achieved between loading axis Z and the 1-o-2 plane. In this case, the uniaxial loading along with Z-axis can be decomposed into the uniaxial loading along with materials axis-1 (fibre direction), axis-2 and axis-3, respectively. Such a loading introduces the out-of-plane stresses into the specimen. The rotation clamps are designed so that it can be easily attached to the inner arms and holes at specific positions at an internal angle of 30°. Both the inner arms and rotation clamps are also made from high strength steel. Each rotation clamp is designed with two parts: one is connected with the inner arm and the other is attached with the specimen through six bolts. Textures are created on the clamp's surfaces in contact with specimens to increase friction.

Once the specimen is loaded, all anti-buckling rails are locked to completely restrict the movement of the outer arms and ensure there is no unexpected loading applied on the specimen when mounting the whole rig into the Instron test machine. After the rig is gripped by the Instron machine, one end of the anti-buckling rail is released to allow the uniaxial movement of each outer arm along the Z-axis direction. The Arcan fixture is originated from M. Arcan et al. [15], known as Arcan's rig, which can achieve an in-plane intersection angle between the uniaxial loading and the principal material direction for the FRP sample, realising the combined tension/shear loading condition with single fixture. After that, some modified versions are proposed to simplify and improve the test. For example, T Laux et al. [16] introduced the loading holes to diversify the stress states and the anti-buckling rails to stabilise the loading process. In the presented novel modified Arcan test rig, rotational clamps are introduced to achieve an out-of-plane intersection angle between the uniaxial loading and the principal material direction for the CFRP sample, therefore, realising the multiple stress combinations with out-of-plane stresses, as shown in Fig. 2.

By changing the relative angles between arms and anti-buckling rails ('C'), and/or interior arms and rotation clamps ('B'), a non-zero angle can be achieved between loading axis Z and the 1-o-2 material plane. In this case, the uniaxial loading along with Z-axis can be decomposed into the uniaxial loading along with axis-1, axis-2 and axis-3, respectively. For the region-of-interest of the specimen, A_{cross}, which is a 5 mm × 5 mm cross-section, this results in two shear stresses and a normal stress, i.e., $\sigma_{z'}$, $\tau_{y'z'}$ and $\tau_{z'x'}$ (see Fig. 3).

The standard basis of local coordinate system of specimen x-y-z is $[e_x\ e_y\ e_z]$. After rotating C and B around x-axis and the z'-axis, respectively, the standard basis of coordinate system x'-y'-z' becomes $[e_{x'}\ e_{y'}\ e_{z'}]$.

We have

$$[e_{x'}\ e_{y'}\ e_{z'}] = \mathbf{R}_x(C)\mathbf{R}_z(B) = \begin{bmatrix} \cos B & -\sin B & 0 \\ \cos C \sin B & \cos C \cos B & -\sin C \\ \sin C \sin B & \sin C \cos B & \cos C \end{bmatrix} \tag{1}$$

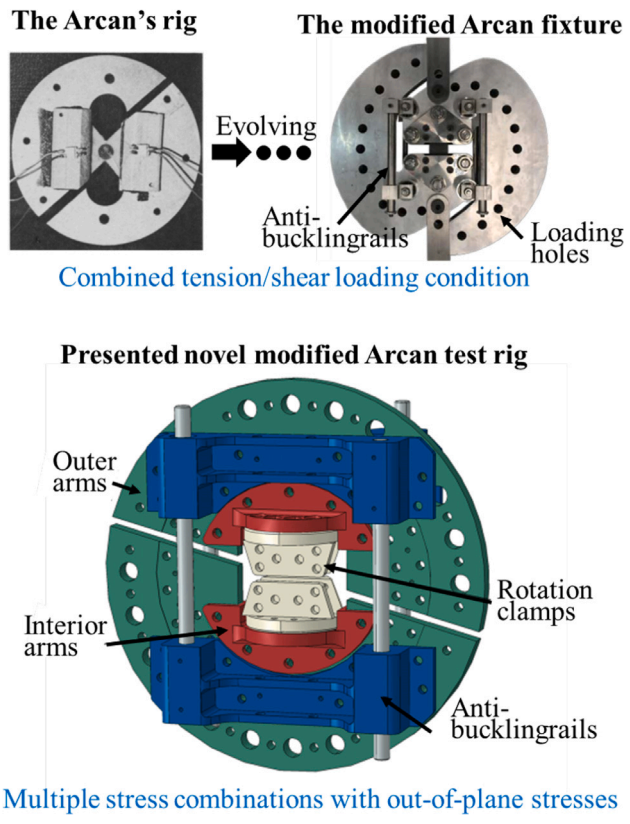

Fig. 2. Comparison of the original Arcan's rig [15], the modified Arcan fixture [16] and the proposed structure design of multiaxial test rig.

where

$$\mathbf{R}_x(C) = \begin{bmatrix} 1 & 0 & 0 \\ 0 & \cos C & -\sin C \\ 0 & \sin C & \cos C \end{bmatrix}, \mathbf{R}_z(B) = \begin{bmatrix} \cos B & -\sin B & 0 \\ \sin B & \cos B & 0 \\ 0 & 0 & 1 \end{bmatrix}$$

are the rotation matrices for vector rotating around the x-axis and z-axis, respectively.

Therefore, there are three non-zero stress components:

$$\begin{cases} \sigma_{x'} = 0; \\ \sigma_{y'} = 0; \\ \sigma_{z'} = F\cos\langle e_z, e_{z'}\rangle / A_{cross} = F\cos C / A_{cross}; \\ \tau_{y'z'} = F\cos\langle e_z, e_{y'}\rangle / A_{cross} = F\sin C\cos B / A_{cross}; \\ \tau_{z'x'} = F\cos\langle e_z, e_{x'}\rangle / A_{cross} = F\sin C\sin B / A_{cross}; \\ \tau_{x'y'} = 0; \end{cases} \tag{2}$$

Furthermore, if the off-axis angle A of the specimen is non-zero, standard basis of coordinate system $x''-y''-z''$ is $[e_{x''}\ e_{y''}\ e_{z''}]$. The Five non-zero stress components in material coordinate system, i.e., σ_1, σ_2, τ_{12}, τ_{31} and τ_{23}, at the centre of the region-of-interest of the specimen can be achieved with stress transformation, $\boldsymbol{\sigma}'' = \boldsymbol{Q}^T\boldsymbol{\sigma}'\boldsymbol{Q}$, where the matrix $\mathbf{Q}$ is

$$\mathbf{Q} = \begin{bmatrix} \cos\langle e_{x'}, e_{x''}\rangle & \cos\langle e_{x'}, e_{y''}\rangle & 0 \\ \cos\langle e_{y'}, e_{x''}\rangle & \cos\langle e_{y'}, e_{y''}\rangle & 0 \\ 0 & 0 & 1 \end{bmatrix}$$

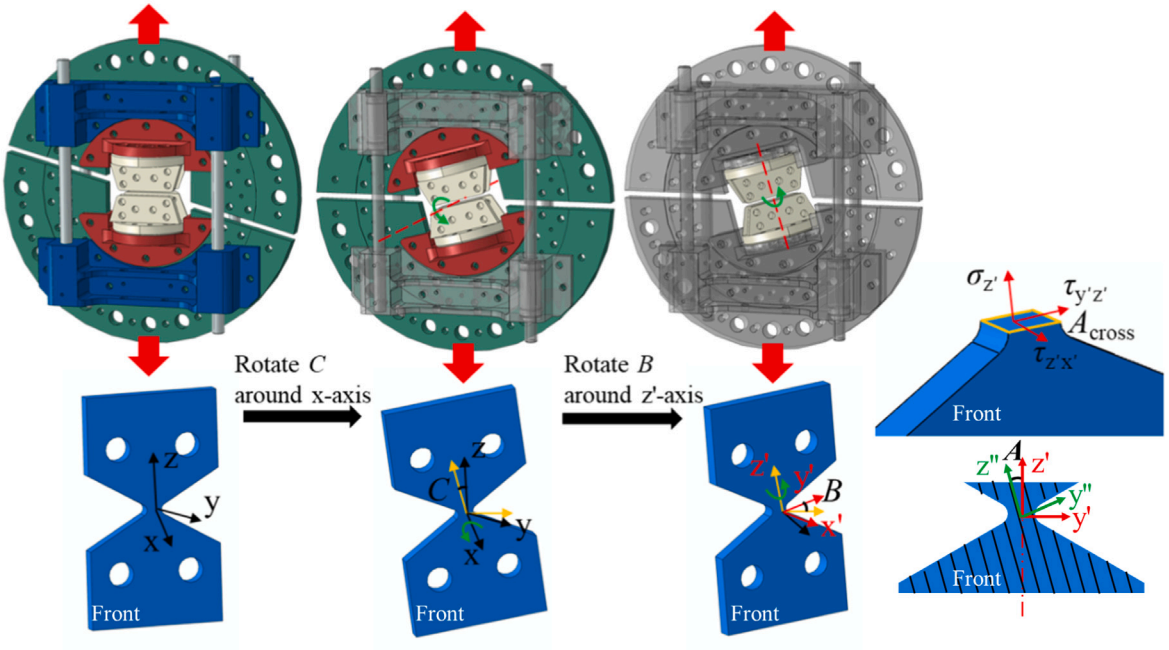

Fig. 3. The fixture with different loading cases.

2.2. Specimen design and manufacturing

The specimen material in this study was the carbon fibre epoxy IM7/8552 prepreg system with a nominal ply thickness of 0.25 mm after autoclave, provided by Hexcel Ltd. The corresponding fibre direction θ with respect to the reference vertical axis of the specimen is illustrated in Fig. 4. Seven variations of UD composite laminae, featuring distinct fibre angles (0°, 15°, 30°, 45°, 60°, 75°, 90°), are produced efficiently using waterjet technology and the manufactured specimens attached to their autoclaved plate are shown in Fig. 4. Such a broad range of unidirectional composites was used to study the applicability of the novel fixture, especially under multiaxial loading conditions. Cross-plied end tab strips made from E-glass fibre-reinforced epoxy composites with the stacking sequence $[+45/-45]_{2s}$ are used alongside a thin XA120 prepreg adhesive film from Easy Composites to allow smooth load transfer from the test machine.

To achieve a reasonably uniform stress distribution and avoid sharp stress concentrations in the region-of-interest of the specimen under multiaxial loading, the width of the specimen is gradually reduced to 5 mm with a notch of a radius of 5 mm at the middle of the specimen, leading to a 5 mm × 5 mm cross-section which is desired to minimise any out-of-plane bending moments. This design allows the load pass through the centre of the region-of-interest (i.e., the cross-section), generating a multiaxial stress state.

2.3. Experimental setup and procedures

The tests were performed using an INSTRON 8802: 250 kN Servo Hydraulic Test Machine. The hydraulic actuator was set to displacement mode. In order to close the gap in the pin fitting of the rig, a small pre-tensile load of roughly 0.5 kN was applied. Then the specimens were loaded at a rate of 0.3 mm/min until the first observable damage occurred mostly from the notch, which in most cases also coincided with the final failure of the specimens.

In order to obtain accurate digital image correlation (DIC) contours, white speckles, of a size of 5–10 pixels, were applied on the upper surface of the specimens. The specimens were carefully aligned to face the camera sensor according to the live image obtained from the camera. Image acquisition was processed using Allied Vision Manta G-146 camera with Canon EF-S 18–55 mm f/3.5–5.6 IS II Lens. DIC was performed using Ncorr v1.2, an open-source 2D DIC MATLAB programme. Prior to testing, the calibration/positioning of the camera is required using a special calibration plate. After pairing the DIC system and the load cell, the load-crosshead displacement data and strain mapping data can be obtained from the Strainsmart data acquisition system and DIC system, respectively. An overview of the experimental setup is found in Fig. 5.

The testing matrix is listed in Table 1. Six types of off-axis tests were conducted to obtain failure stresses ($\sigma_{11}, \sigma_{22}, \sigma_{12}$) and were verified by Tsai–Hill failure criterion. Another set of biaxial tests were carried out on unidirectional composite specimens to validate the RVE models in the stress space (σ_{11}, σ_{12}). Finally, multiaxial loading conditions were applied to unidirectional composites and the extracted stress ($\sigma_{11}, \sigma_{22}, \sigma_{12}, \sigma_{13}, \sigma_{23}$) at the peak load were applied to the RVE model for failure analysis and comparisons. The representative tested samples were scanned using X-ray computed microtomography Zeiss Xradia 620 (National X-ray Imaging Centre, Manchester). The scanned 2D images were reconstructed using Zeiss built-in programme and visualised using Avizo.

3. Micromechanical modelling of composites

3.1. 3D RVE model

Computational micromechanics was proven to be an efficient tool to study the progressive failure of UD composite under uniaxial loads [17–21], combined transverse tension/compression and in-plane shear [17,22], combined longitudinal compression and in-plane shear [23] and triaxial loads [24,25] . In this study, the RVE model was generated for the progressive failure analysis of unidirectional composites under multiaxial loading conditions. Three constituents, namely the fibre, matrix and fibre/matrix interface, were accounted for in the RVE model. An average diameter of fibres was set to 5.3–7 μm and 50 carbon fibres were generated based on a shaking model and experimental data using a discrete element method [26], resulting in a volume fraction of fibres to be 60%. The size of the cross section of the RVE is 50 μm × 50 μm and its depth is 5 μm to compromise between the precision of the numerical results and computational time. The fibres and matrix in the RVE

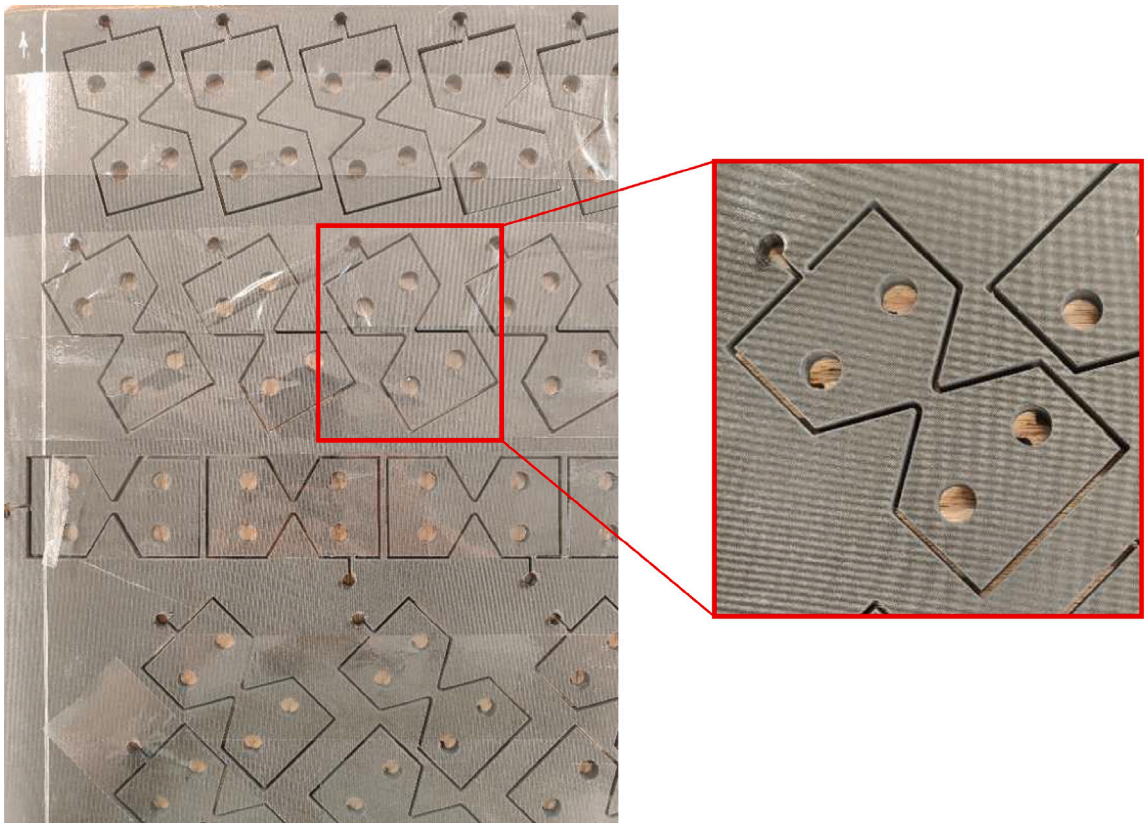

Fig. 4. Manufactured specimens with water-jetting in their autoclaved plate.

Table 1
Testing matrix.

Loading configuration	A	B	C	Multiaxial stresses	Number of specimens
Off-axis tests					
1	15	0	0	$(\sigma_{11}, \sigma_{22}, \sigma_{12})$	2
2	30	0	0	$(\sigma_{11}, \sigma_{22}, \sigma_{12})$	2
3	45	0	0	$(\sigma_{11}, \sigma_{22}, \sigma_{12})$	2
4	60	0	0	$(\sigma_{11}, \sigma_{22}, \sigma_{12})$	2
5	75	0	0	$(\sigma_{11}, \sigma_{22}, \sigma_{12})$	2
6	90	0	0	$(\sigma_{11}, \sigma_{22}, \sigma_{12})$	2
Biaxial tests					
7	0	0	15	$(\sigma_{11}, \sigma_{12})$	2
8	0	0	30	$(\sigma_{11}, \sigma_{12})$	2
9	0	0	45	$(\sigma_{11}, \sigma_{12})$	2
10	0	0	60	$(\sigma_{11}, \sigma_{12})$	2
11	0	0	75	$(\sigma_{11}, \sigma_{12})$	2
12	0	0	90	$(\sigma_{11}, \sigma_{12})$	2
Multiaxial tests					
13	15	30	30	$(\sigma_{11}, \sigma_{22}, \sigma_{12}, \sigma_{13}, \sigma_{23})$	2
14	15	45	45	$(\sigma_{11}, \sigma_{22}, \sigma_{12}, \sigma_{13}, \sigma_{23})$	1
15	30	15	30	$(\sigma_{11}, \sigma_{22}, \sigma_{12}, \sigma_{13}, \sigma_{23})$	1
16[a]	30	30	45	$(\sigma_{11}, \sigma_{22}, \sigma_{12}, \sigma_{13}, \sigma_{23})$	1
17	45	15	45	$(\sigma_{11}, \sigma_{22}, \sigma_{12}, \sigma_{13}, \sigma_{23})$	1
18	45	15	0	$(\sigma_{11}, \sigma_{22}, \sigma_{12}, \sigma_{13}, \sigma_{23})$	1
19[a]	60	45	15	$(\sigma_{11}, \sigma_{22}, \sigma_{12}, \sigma_{13}, \sigma_{23})$	1
20	60	15	30	$(\sigma_{11}, \sigma_{22}, \sigma_{12}, \sigma_{13}, \sigma_{23})$	1
21	75	15	30	$(\sigma_{11}, \sigma_{22}, \sigma_{12}, \sigma_{13}, \sigma_{23})$	1

[a] Specimens which were CT scanned for post-failure inspection.

were discretised with first-order hexahedral elements under a reduced integration scheme (C3D8R) and a few tetrahedral elements (C3D6), while the fibre/matrix interface was meshed with first-order cohesive elements (COH3D8). Fig. 6a illustrates the microstructure of the 3D RVE model of a UD composite lamina with three material constituents. Approximately 20,000 elements were used for the discretisation of the RVE in ABAQUS/Explicit. The stable time increment was set to 5×10^{-6} s to accelerate numerical computation.

3.2. Constitutive models of constituents and mechanical properties

Carbon fibres were modelled as linearly elastic and transversely isotropic and assumed to not contribute to the failure of the composite under multiaxial loads that are dominated by transverse and shear loadings. In line with previous work [24,25], the polymer matrix was modelled as an isotropic elastoplastic solid. The modified Drucker–Prager plastic damage model [27] was used to model the mechanical behaviour of epoxy under multiaxial stress states. Regarding the mechanical behaviour of the matrix under uniaxial tension, the quasi-brittle behaviour was controlled by an exponential cohesive law after the onset of damage, characterised by a single normalised scalar damage variable d, to ensure correct energy dissipation of the matrix G_m; while under uniaxial compression, perfect plasticity was assumed based on experimental findings [28], which is shown in Fig. 6(b). More details about the constitutive models and the numerical implementation can be found in [21,22,24,25].

The mechanical behaviour of the fibre/matrix interface was modelled with a bilinear cohesive model using cohesive elements. The machine learning based approach was used to determine the penalty stiffnesses [29]. A quadratic stress interaction criterion was used to predict the onset of damage. The calibrated interface strengths in normal and shear directions from our previous study [25] were 58 MPa and 92 MPa, respectively. The interface fracture energy in mode I, G_{IC} was assumed as 2 J/m^2 and the fracture energies in mode II/III is assumed to be equal to the matrix cracking fracture energy, 100 J/m^2 [22,25]. Material properties can be found in Table 2.

Uncertain material properties including the stiffness and thickness of the fibre/matrix interface region as well as the transverse modulus

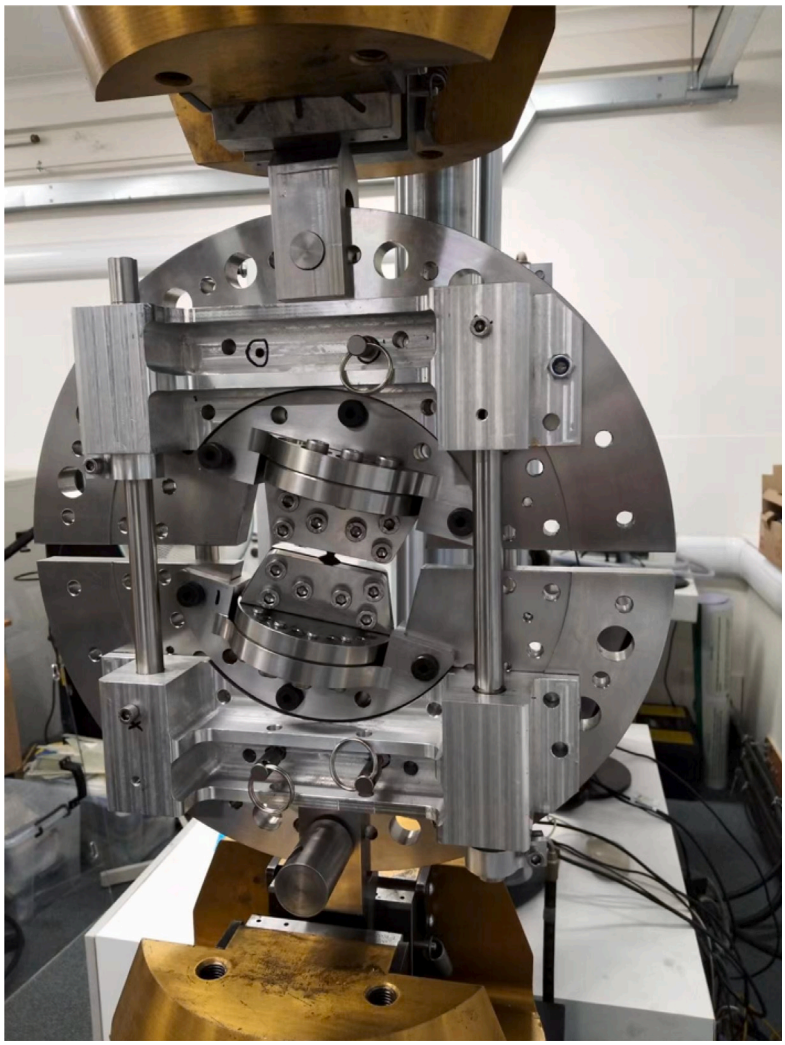

Fig. 5. Overview of the modified Arcan fixture experimental setup.

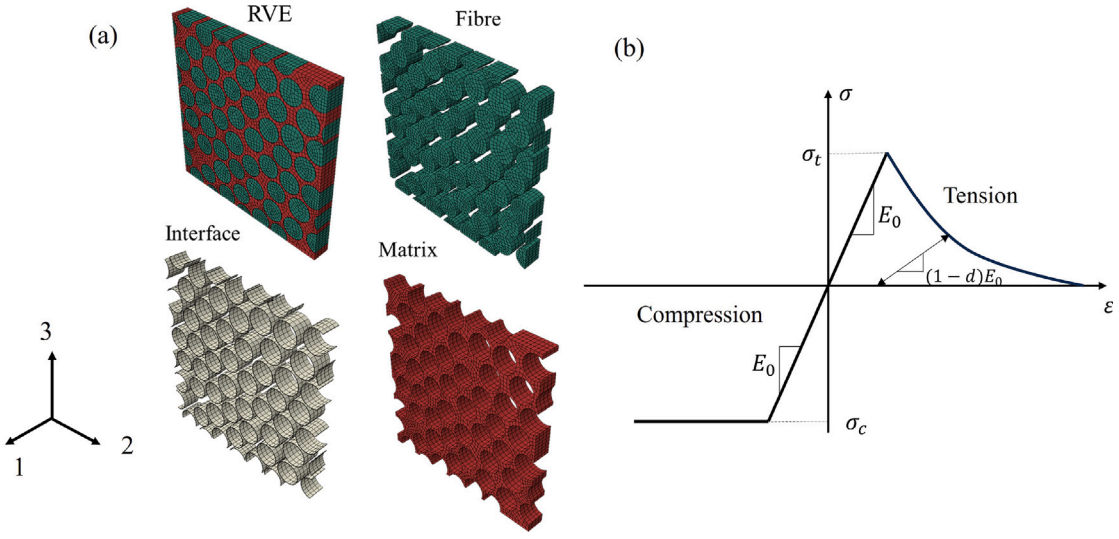

Fig. 6. (a) Three-phase based RVE model set-up and (b) Constitutive model of 8552 epoxy.

Table 2
Material properties of the fibre, matrix and interface.

IM7 carbon fibre					
E_1 (GPa)	$E_2 = E_3$ (GPa)	$\nu_{12} = \nu_{13}$	ν_{23}	$G_{12} = G_{13}$ (GPa)	G_{23} (GPa)
287	13.34	0.29	0.48	23.8	7
8552 epoxy					
E (GPa)	ν	σ_t (MPa)	σ_c (MPa)	G_m (J/m^2)	
4.08	0.38	99	130	100	
Interface					
K_n (GPa/mm)	$K_{s/t}$ (GPa/mm)	t_n^0 (MPa)	$t_{s/t}^0$ (MPa)	G_{IC} (J/m^2)	$G_{IIC/IIIC}$ (J/m^2)
682	253	58	92	2	100

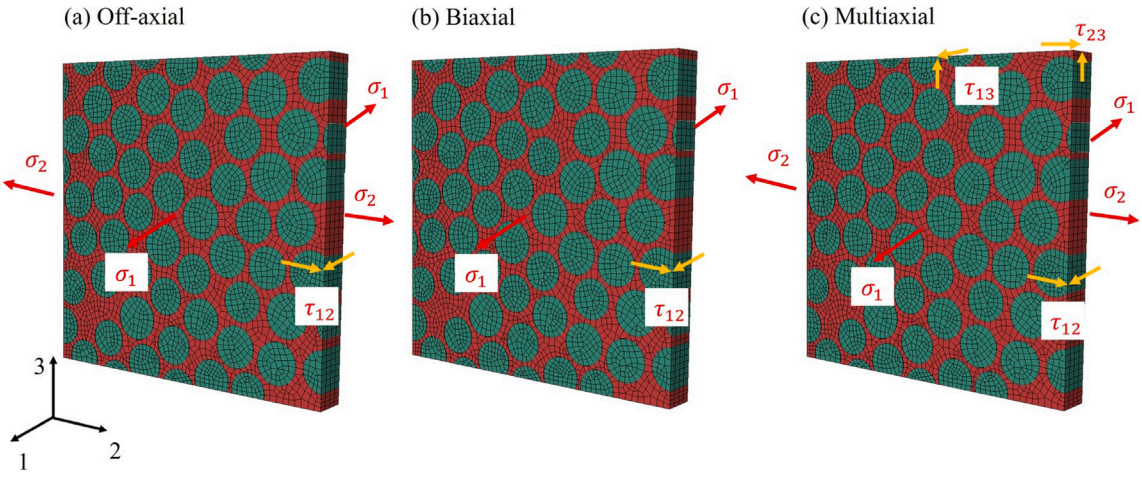

Fig. 7. Loading conditions with different stress configurations: (a) Off-axial, (b) Biaxial and (c) Multiaxial stresses.

of carbon fibres were numerically identified using the artificial neural network (ANN) [29]. A single fibre unit cell FE model for each selected composites and use cohesive zone model (CZM) for the fibre/matrix interface was developed. An ANN was first trained by FE modelling inputs (i.e., uncertain constituent properties and interphase thickness) and outputs (i.e., experimentally measured UD lamina properties). Design of Experiments (DoE) techniques, including Optimal Latin Hypercube (OLH) sampling were used to define the training points of the ANN. Once trained the ANN was used to construct surrogate metamodels to identify the uncertain material constituent properties that lead to the closest lamina properties as compared with experimental data.

3.3. Periodic boundary conditions and loading cases

Periodic boundary conditions (PBCs) were imposed on the periodic nodes on the opposite faces of the RVE to guarantee the periodicity of displacement and traction. The resultant strains were calculated from the imposed displacement divided by the corresponding lengths, while the resultant normal and shear stresses were calculated from the resultant normal and tangential forces acting on the RVE's faces divided by the cross-sectional area. Fig. 7 shows the configuration of off-axial, biaxial, and multiaxial loading stress imposed on the RVE. The imposed strains obtained from the experiments were calculated from the decoupled stresses at the failure point using Hook's law.

4. Verification of multiaxial rig using off-axial and biaxial tensile tests

4.1. Off-axis tensile tests

The multiaxial rig can be retrieved to the conventional off-axial tests by setting both the outer arm and the rotation clamp angles to 0° with specimens cut at different angles with respect to the fibre direction. Unidirectional laminates with and without the rig were tested for comparison and the stress–strain curves can be found in Fig. 8. Failure strength was obtained as 295 MPa without the multiaxial rig due to the failure mode was fibre/matrix debonding initiated from the notch, which is not fibre breakage as expected. The stiffness obtained from UD composites was found smaller than the one obtained without the rig, which is mainly due to the gap and less friction between the specimens and clamp. The failure strength was not obtained from the tests with the rig, thus only the matrix failure dominated tests with the fibre angles of 45°, 75° and 90° specimens were used to obtain the failure strength. Matrix cracking initiated from the notch and propagated along the fibre direction, leading to a clear fracture plane, see Fig. 9. Photos of failure modes of the off-axis tests are also included Figs. 8–9 where A represents the fibre angle.

The in-situ strength of the off-axis laminae under uniaxial tension are calculated by dividing the peak load over the 5 mm × 5 mm cross-section. The average failure strength and coefficient of variation (CV) for 45°, 75° and 90° specimens are listed in Table 3. The experimental average failure strength of unidirectional 45° specimens obtained with the multiaxial rig is 16% larger than the one obtained from literature [30], with 3% small deviation. However, the transverse tensile strength measured from the 90° specimens is 38% smaller than the one in literature [30,31], which may be due to the sensitivity of matrix failure towards the unwanted stress generated by the complex multiaxial structure. Nevertheless, 22.6% deviation is still observed for the transverse tensile strength, even in the conventional ASTM Standard testing. In this study, 62 MPa was used for the plot of failure strength-fibre angle for Tsai–Hill failure criterion in comparison with the experimental data obtained from the multiaxial testing rig and literature [30,31]. Tsai–Hill failure criterion predicts slightly conservative stresses to cause failure for 15° and 30° off-axis specimens, while good agreement between the theoretical predictions and experimental data

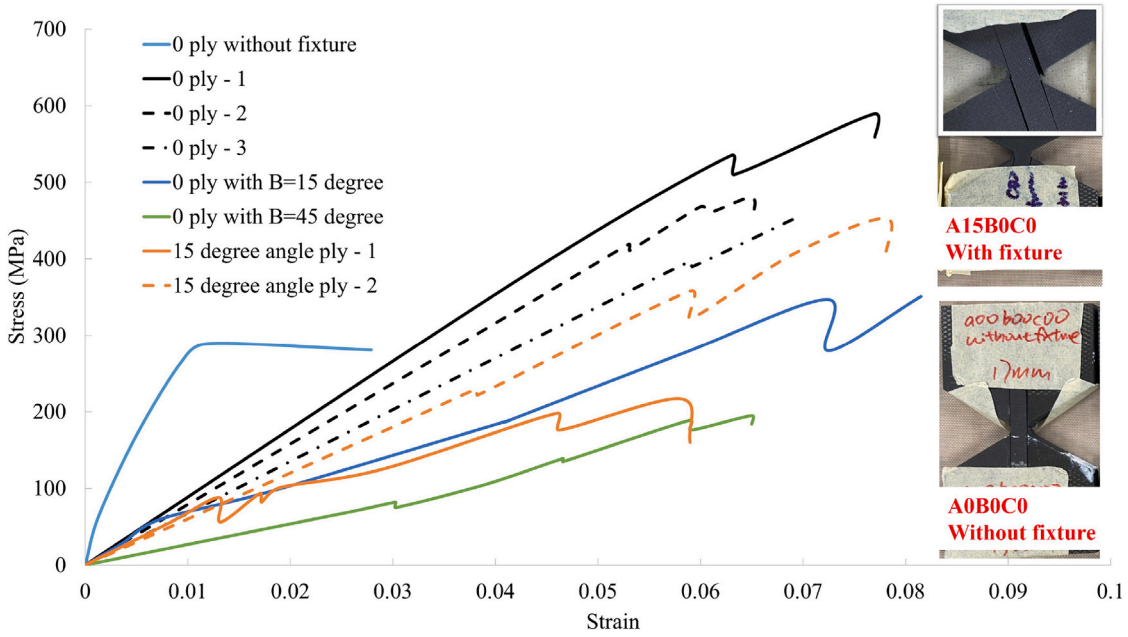

Fig. 8. Stress–strain curves of UD composites with and without fixture and 15° off-axis composites under tensile loading.

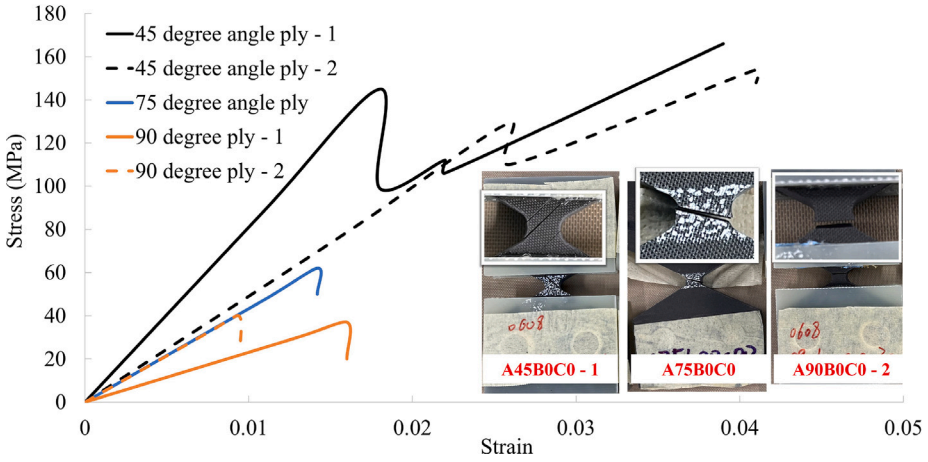

Fig. 9. Stress–strain curves of 45°, 75° and 90° off-axis composite specimens under tensile loading.

Table 3
The comparison of experimental failure strength of 45°, 75° and 90° angled unidirectional IM7/8552 composites against the ones from literature [30,31].

Ply angle	Avg. strength (MPa)	CV	Avg. strength Refs (MPa)	CV Refs
45°	136.5	5.4%	114 [30]	8.3% [30]
75°	62	–	–	–
90°	38.5	3.9%	62 [30,31]	22.6% [30], 8.5% [31]

can be found for 45° and 75° off-axis specimens under tensile tests (see Fig. 10)

4.2. Biaxial tensile tests

Biaxial longitudinal tension and in-plane shear tests were carried out using UD laminae under different outer arm angles including 15°, 30°, 45°, 60° and 75°. The pure in-plane shear tests were also performed by changing the outer arm angle to 90°. Typical biaxial stress–strain curves of testing with different outer arm angles are shown in Figs. 11–12. The resultant stress is calculated from the peak load over the 5 mm × 5 mm cross-section and the strain is calculated from the displacement over the length of the specimen which is not covered by the glass fibre-reinforced composites tab. Still, the peak loads of the specimens with the outer arm angle not greater than 45° were not obtained at final failure due to the matrix cracking along fibres from the notch edges, see Fig. 11. Matrix cracking initiated from the notch edge around 120 MPa for aforementioned three cases. Shear failure starts to play an important role under biaxial loadings for the specimens with the fibre angle of 60° and 75°, although matrix cracking can still be found around 80 MPa and 100 MPa, corresponding to the fluctuations on the curves, respectively. Nonlinearity due to matrix yielding is observed for the pure in-plane shear case, where no matrix cracking was found around the edge. RVE modelling was conducted for the in-plane shear where the load is perpendicular to the fibre direction. Good agreement is found between experimental data and numerical

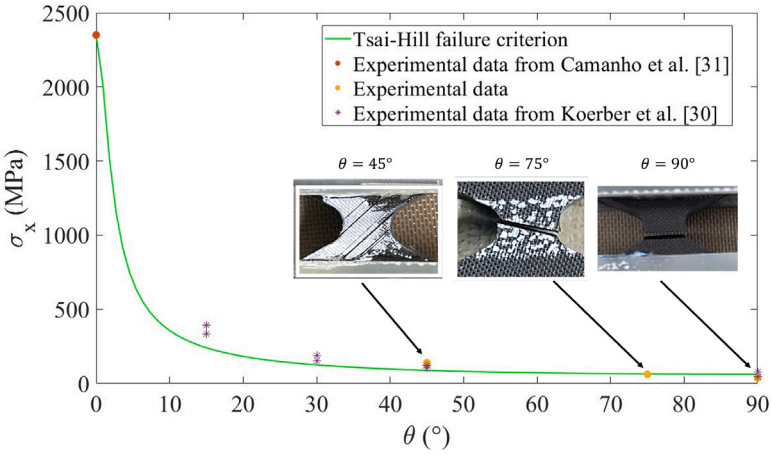

Fig. 10. Comparison of off-axis tensile strength predicted by Tsai–Hill failure criterion and experimental tests [30,31].

simulation regarding the elasticity and failure strength, see Fig. 12. Strain hardening effect due to fibre rotation was successfully predicted by the RVE model, and the difference between the experimental and numerical curves may result from the length of fibres within the RVE model, which generated extensive plastic deformation under shear perpendicular to fibres [32].

The in-situ biaxial failure strength of the UD laminae is determined by resolving the maximum uniaxial load in normal and tangential directions for the respective tensile and shear strengths, according to Eq. (2). The biaxial strengths are plotted against the failure envelopes predicted by analytical models (i.e., Hashin, Tsai–Wu, Tsai–Hill, LaRC05 and Maximum principal stress failure criteria) and numerical simulations in Fig. 13. The longitudinal tensile failure strength of 2350 MPa is adopted from the literature [30,31] for the plot of failure envelopes and pure in-plane shear strengths from the literature [30,31,33] are also plotted for comparison. Compared with these failure criteria, the measured biaxial tensile-shear failure strength of UD laminae is slightly larger than the ones obtained numerically and analytically. Due to the limitation of the fixture on biaxial stress ratios, RVE models were adopted to explore more possibilities of failure strengths with wider stress ratios. Shear perpendicular and parallel to fibres are adopted for the exploration of failure strength under biaxial longitudinal tension and shear. It can be found that failure strength obtained from longitudinal tension and shear parallel to fibres has a constant component of shear strength, which is close to the pure shear strength. However, when longitudinal tension and shear perpendicular to fibres is applied, an increase in shear strength is predicted when longitudinal strength increases. This is mainly due to the rotation of fibres under pure shear perpendicular to fibres. This trend is also found in the failure envelope for UD composite lamina tube made of T300/BSL914C under longitudinal and shear tests [34]. Such failure mechanism is not considered in current failure criteria, although interactive Tsai–Wu failure criterion has a similar trend. Good agreement is found between numerical simulations with the in-plane shear parallel to fibres and predictions from LaRC05 and the maximum stress failure criteria considering shear dominated failure in the biaxial loadings. Fibre breakages were not taken into account in this study due to the limitation of the current RVE model, so dashed lines are plotted instead for the comparison of failure envelopes with possible fibre breakage-dominated failure.

5. Failure analysis of UD composites under multiaxial loading

Figs. 14 and 15 show the typical stress–strain curves for UD CFRP specimens under different multiaxial loading conditions. A15B30C30 represents the 15° off-axis specimen is loaded with the rotation angle of clamps as 30° and the rotation angle of outer arms as 30°. First disturbance on the curves indicates the first matrix cracking initiated from the edge of the notch when the fibre angle is not greater than 45°. Since the cracking path does not pass through the designate centre of the specimen, it is challenging to obtain the final strength under multiaxial loading. Stress–strain curves with larger fibre angles (i.e., 60° and 75°) witness a brittle failure with some yielding process. This is mainly because the failure modes of the specimen under those multiaxial stress states are matrix cracking and fibre/matrix interface debonding. Fig. 16 shows the strain contours from DIC at initial loading and final failure, and the final failure model obtained from CT scanning for cases A60B45C15 and A30B30C45. For both off-axis specimens under multiaxial loadings, it was found that initial strain concentration mainly occurs at the edge close to the clamps and final failure was found at the notch along the fibre directions. Matrix cracking initiated from the edge of notch and resulted in fibre splitting towards the edge of specimens and stopped by the clamps (see Fig. 17)

The influences of fibre angle on the mechanical performance under a specific stress state (B = C = 15°) is also studied with a range of fibre angle from 15° to 75°. It can be found that the specimens with fibre angle of 15° and 30° share same Young's Modulus due to the small difference of fibre angle and the Modulus decreases as the fibre angle increases. It is challenging to predict the failure strength of the specimens with fibre angle of 15° and 30° since fibres started to hold the load until the matrix cracking propagated into the grip sections. The failure strength with the fibre angle of 60° and 75° are predicted and it reduced by 52% when the angle increases from 60° to 75°.

Numerical simulation were conducted to predict stress states of the RVE with the same loading conditions as in experimental test for cases A75B15C30 and A60B15C15. It should be noted that RVE modelling is used to predict the stress states at the centre of the specimen with an assumption that the specimen is elastic brittle. Due to the existence of notch, a scale factor of four calculated from the finite element stress analysis is selected to scale up the displacements calculated from the measured failure strength. The failure strength measured from the multiaxial loading cases A75B15C30 and A60B15C15 is compared to the corresponding numerical results predicted by RVE model in Table 4, which shows reasonable agreement from the perspective of strength ratio of different stress components over the longitudinal stress.

6. Conclusions

This study proposed a novel fig for testing UD CFRP laminae under multiaxial loading conditions, which could be extended for composite laminates. The test rig with a rotational clamp was developed to enable multiple stress combinations with out-of-plane stresses in UD laminae on a traditional laboratory-based uniaxial test machine. The test rig was verified by off-axis tension and validated by biaxial longitudinal tension

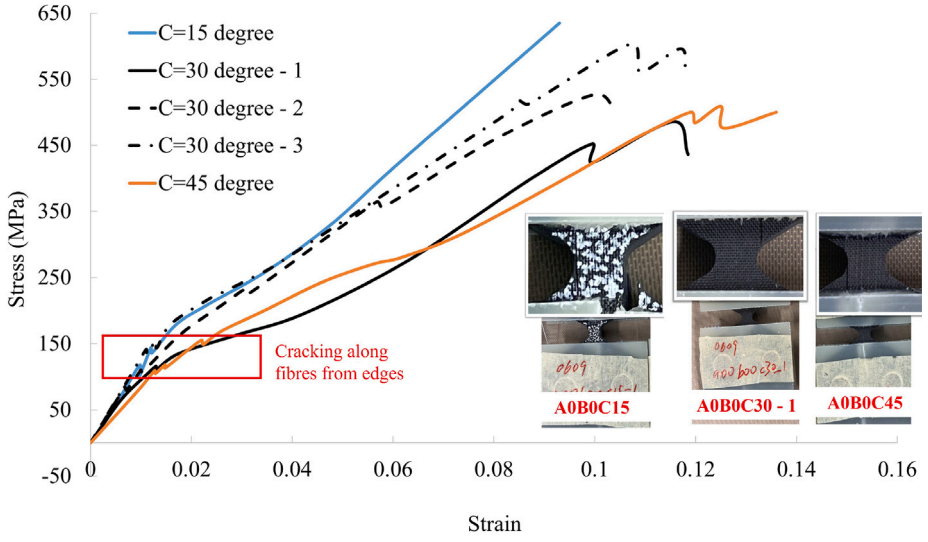

Fig. 11. Stress–strain curves of UD composites under biaxial tensile loading with an outer arm angles of 15°, 30° and 45°.

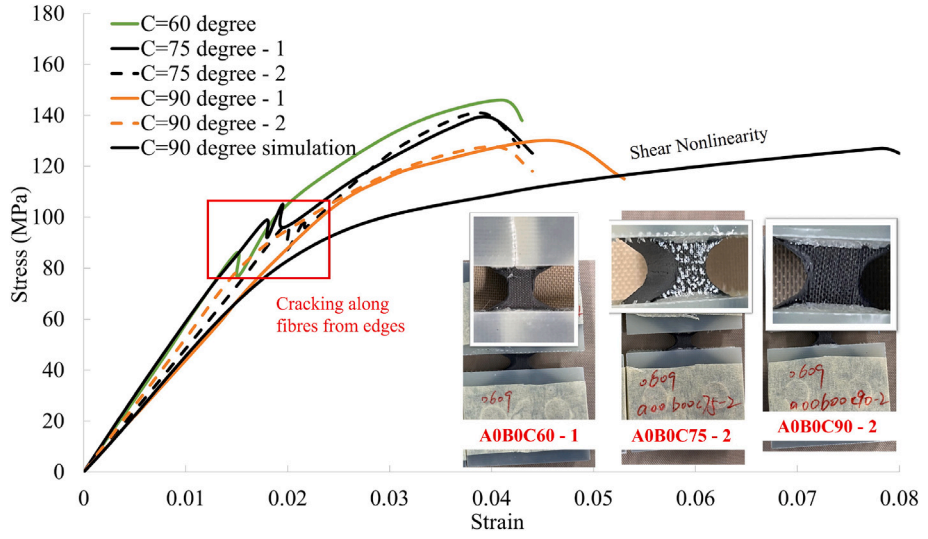

Fig. 12. Stress–strain curves of UD composites under biaxial tensile loading with an outer arm angles of 60°, 75° and 90°.

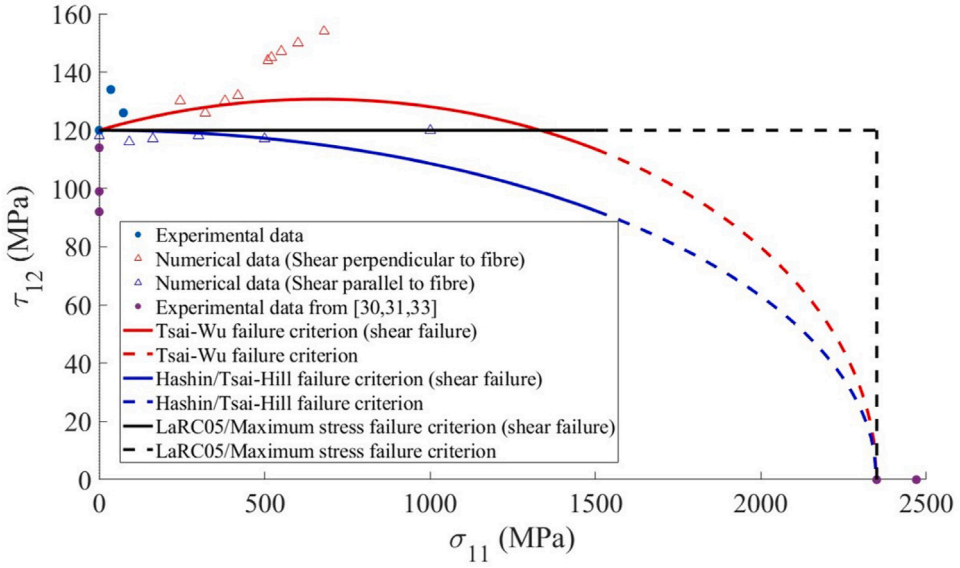

Fig. 13. Comparison of failure envelope of UD IM7/8552 composites predicted by conventional failure criteria and RVE models against experimental data obtained with the rig under longitudinal tension and in-plane shear.

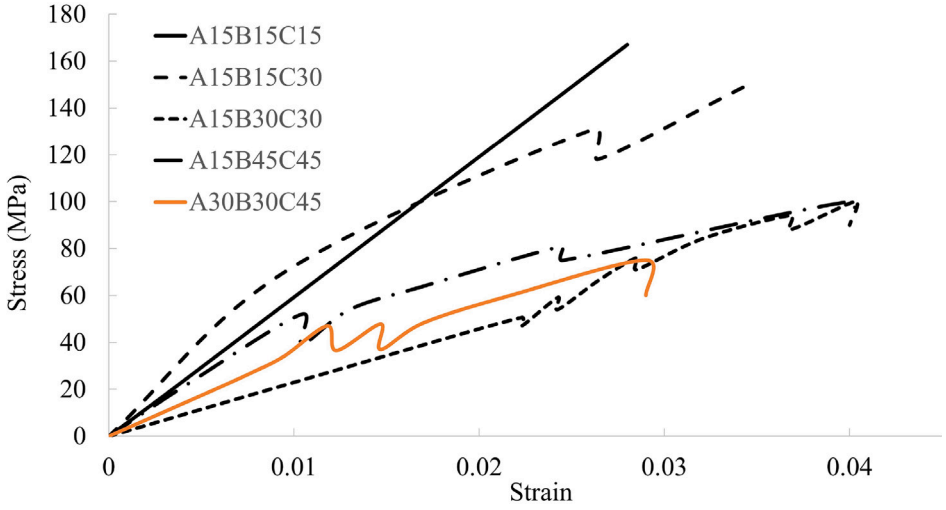

Fig. 14. Stress–strain curves of 15° and 30° off-axis composite specimens under multiaxial loading conditions. (A is the fibre angle, B is the rotation angle of clamps and C is the rotation angle of outer arms.).

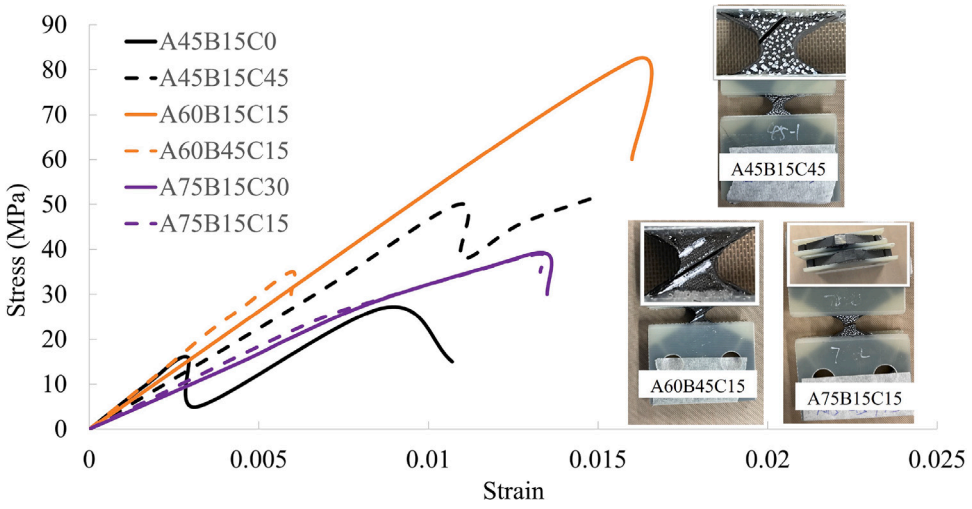

Fig. 15. Stress–strain curves of 45°, 60° and 75° off-axis composite specimens under multiaxial loading conditions. (A is the fibre angle, B is the rotation angle of clamps and C is the rotation angle of outer arms.).

Table 4
Comparison between experimental data and numerical prediction for multiaxial loading cases A75B15C30 and A60B15C15.

Multiaxial case	Experimental testing	RVE-based FEM prediction
A75B15C30	(σ_{11} = 7.3 MPa)	(σ_{11} = 9.4 MPa)
$(1, \frac{\sigma_{22}}{\sigma_{11}}, \frac{\sigma_{12}}{\sigma_{11}}, \frac{\sigma_{13}}{\sigma_{11}}, \frac{\sigma_{23}}{\sigma_{11}})$	(1, 5.75, 1.1, −0.18, 0.68)	(1, 4.6, 0.98, −0.15, 0.55)
A60B15C15	(σ_{11} = 2 MPa)	(σ_{11} = 2.1 MPa)
$(1, \frac{\sigma_{22}}{\sigma_{11}}, \frac{\sigma_{12}}{\sigma_{11}}, \frac{\sigma_{13}}{\sigma_{11}}, \frac{\sigma_{23}}{\sigma_{11}})$	(1, 38.5, −12, 1.38, 2.38)	(1, 26.7, −10, 1.39, 2.6)

and shear perpendicular to fibres. UD CFRP laminae were tested, for the first time, under five stress combinations using the test rig, with results cross-validated against a high-fidelity representative volume element (RVE)-based 3D micromechanical finite element model. Failure strength envelope and damage mechanisms demonstrate reasonable applicability of the test rig for composite failure under multiaxial loading conditions with a broad spectrum of stress combinations.

Due to the limitation of loading capability, the test rig is currently not applicable for testing on off-axis specimens with the fibre angle smaller than 45% as well as the UD laminae with the rotation angle of the outer arm not greater than 45%. Further improvement and protoyping is still required. However, thinner CFRP composites or customised glass fibre reinforced polymer composites with lower longitudinal failure strength could be considered for testing in our future work to capture the composite failure with fibre breakage.

CRediT authorship contribution statement

Lei Wan: Writing – review & editing, Writing – original draft, Software, Methodology, Formal analysis, Data curation, Investigation. **Ka Zhang:** Methodology, Investigation, Conceptualization. **Jiayun Chen:** Writing – original draft, Methodology, Data curation, Conceptualization. **Aonan Li:** Methodology, Investigation, Data curation. **Jiang Wu:** Software, Methodology, Investigation. **Dongmin Yang:** Writing – review & editing, Writing – original draft, Supervision, Project administration, Methodology, Funding acquisition, Conceptualization.

Declaration of competing interest

The authors declare that they have no known competing financial interests or personal relationships that could have appeared to influence the work reported in this paper.

Acknowledgements

This work was supported by the UK Engineering and Physical Sciences Research Council (EPSRC) IAA grant number PIV051. This

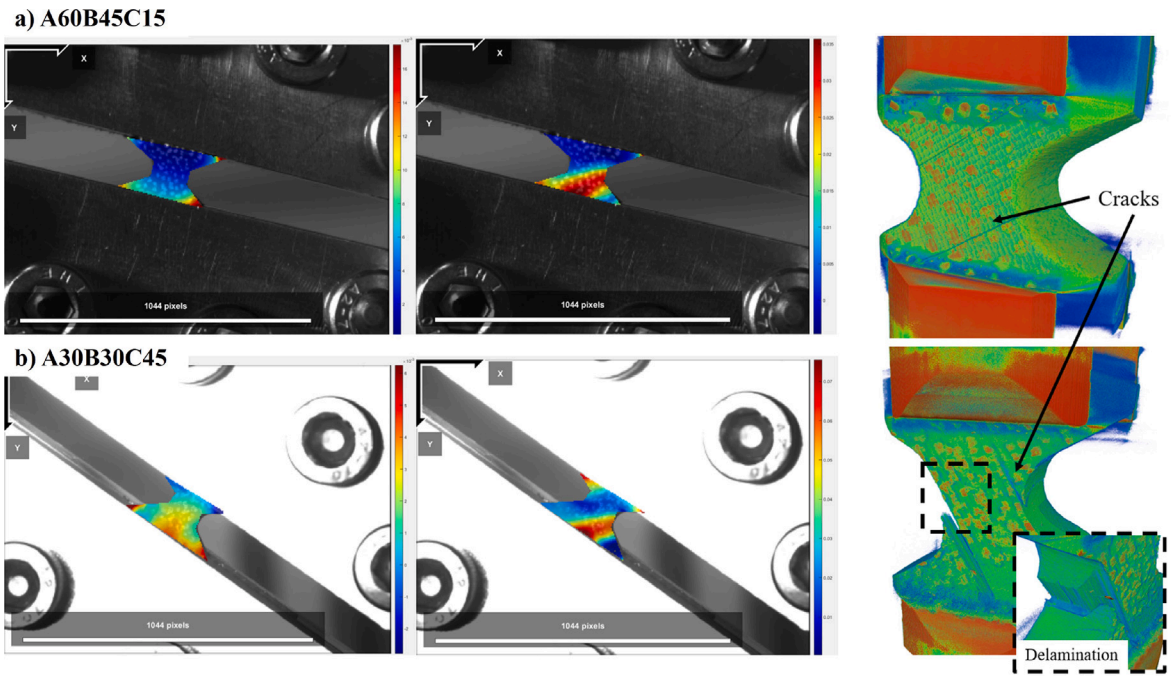

Fig. 16. Failure characterisation with DIC (left) and CT scans (right) for case A60B45C15 and A30B30C45.

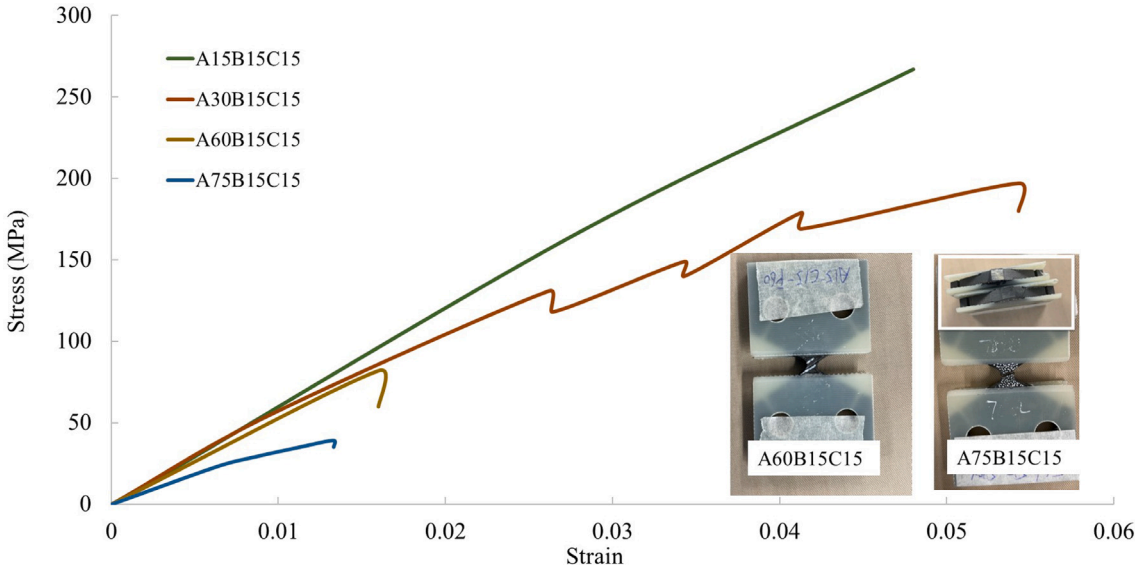

Fig. 17. Stress–strain of angle ply composites under a specific multiaxial stress state (B = C = 15°).

work was also supported by the National Research Facility for Lab X-ray CT (NXCT) through EPSRC, United Kingdom grant EP/T02593X/1. The authors acknowledge Hexcel for kindly providing the IM7/8552 composites for the tests and the School of Engineering workshop for machining the multiaxial test rig.

Data availability

Data will be made available on request.

References

[1] Tsai SW, Wu EM. A general theory of strength for anisotropic materials. J Compos Mater 1971;5(1):58–80.
[2] Hashin Z. Failure criteria for unidirectional fiber composites. J Appl Mech 1980;47(2):329–34.
[3] Puck A, Schürmann H. Failure analysis of FRP laminates by means of physically based phenomenological models. Compos Sci Technol 1998;58(7):1045–67.
[4] Pinho S, Iannucci L, Robinson P. Physically-based failure models and criteria for laminated fibre-reinforced composites with emphasis on fibre kinking: Part I: Development. Compos A: Appl Sci Manuf 2006;37(1):63–73.
[5] Kaddour A, Hinton M. Maturity of 3D failure criteria for fibre-reinforced composites: Comparison between theories and experiments: Part B of WWFE-II. J Compos Mater 2013;47(6–7):925–66.
[6] Gan KW, Laux T, Taher ST, Dulieu-Barton JM, Thomsen OT. A novel fixture for determining the tension/compression-shear failure envelope of multidirectional composite laminates. Compos Struct 2018;184:662–73.
[7] Vogler T, Hsu S-Y, Kyriakides S. Composite failure under combined compression and shear. Int J Solids Struct 2000;37(12):1765–91.
[8] Cognard J-Y, Sohier L, Davies P. A modified Arcan test to analyze the behavior of composites and their assemblies under out-of-plane loadings. Compos A: Appl Sci Manuf 2011;42(1):111–21.

[9] Vogler T, Kyriakides S. Inelastic behavior of an AS4/PEEK composite under combined transverse compression and shear. Part I: experiments. Int J Plast 1999;15(8):783–806.
[10] Zheng T, Huang J, Guo L, Sun R, Huang T, Zhou J, Jia F, Hong C. A combined experimental and numerical approach to investigate the failure behaviors of 3D woven composites under biaxial tensile loading. Compos Sci Technol 2023;236:109974.
[11] Bing Q, Sun C. Specimen size effect in off-axis compression tests of fiber composites. Compos B: Eng 2008;39(1):20–6.
[12] Nemeth MP, Herakovich CT, Post D. On the off-axis tension test for unidirectional composites. Compos Technol Res 1983;5(2):61–8.
[13] Welsh J, Adams D. Development of an electromechanical triaxial test facility for composite materials. Exp Mech 2000;40:312–20.
[14] Zinoviev PA, Tsvetkov SV, Kulish GG, van den Berg RW, Van Schepdael LJ. The behavior of high-strength unidirectional composites under tension with superposed hydrostatic pressure. Compos Sci Technol 2001;61(8):1151–61.
[15] Arcan M, Hashin Z, Voloshin A. A method to produce uniform plane-stress states with applications to fiber-reinforced materials: a specially designed specimen yields material properties under pure shear or uniform plane-stress conditions. Exp Mech 1978;18:141–6.
[16] Laux T, Gan KW, Dulieu-Barton JM, Thomsen OT. Ply thickness and fibre orientation effects in multidirectional composite laminates subjected to combined tension/compression and shear. Compos A: Appl Sci Manuf 2020;133:105864.
[17] Wan L, Ismail Y, Zhu C, Zhu P, Sheng Y, Liu J, Yang D. Computational micromechanics-based prediction of the failure of unidirectional composite lamina subjected to transverse and in-plane shear stress states. J Compos Mater 2020;54(24):3637–54.
[18] Vaughan T, McCarthy C. Micromechanical modelling of the transverse damage behaviour in fibre reinforced composites. Compos Sci Technol 2011;71(3):388–96.
[19] Varandas LF, Catalanotti G, Melro A, Tavares R, Falzon BG. Micromechanical modelling of the longitudinal compressive and tensile failure of unidirectional composites: The effect of fibre misalignment introduced via a stochastic process. Int J Solids Struct 2020;203:157–76.
[20] Yang L, Wu Z, Cao Y, Yan Y. Micromechanical modelling and simulation of unidirectional fibre-reinforced composite under shear loading. J Reinf Plast Compos 2015;34(1):72–83.
[21] Naya F, Herráez M, Lopes C, González C, Van der Veen S, Pons F. Computational micromechanics of fiber kinking in unidirectional FRP under different environmental conditions. Compos Sci Technol 2017;144:26–35.
[22] Naya F, González C, Lopes C, Van der Veen S, Pons F. Computational micromechanics of the transverse and shear behavior of unidirectional fiber reinforced polymers including environmental effects. Compos A: Appl Sci Manuf 2017;92:146–57.
[23] Sun Q, Zhou G, Meng Z, Guo H, Chen Z, Liu H, Kang H, Keten S, Su X. Failure criteria of unidirectional carbon fiber reinforced polymer composites informed by a computational micromechanics model. Compos Sci Technol 2019;172:81–95.
[24] Chen J, Wan L, Ismail Y, Hou P, Ye J, Yang D. Micromechanical analysis of UD CFRP composite lamina under multiaxial loading with different loading paths. Compos Struct 2021;269:114024.
[25] Chen J, Wan L, Ismail Y, Ye J, Yang D. A micromechanics and machine learning coupled approach for failure prediction of unidirectional CFRP composites under triaxial loading: A preliminary study. Compos Struct 2021;267:113876.
[26] Ismail Y, Yang D, Ye J. Discrete element method for generating random fibre distributions in micromechanical models of fibre reinforced composite laminates. Compos B: Eng 2016;90:485–92.
[27] Systèmes D. Abaqus documentation. Providence, RI: Dassault Systèmes; 2014.
[28] Fiedler B, Hojo M, Ochiai S, Schulte K, Ando M. Failure behavior of an epoxy matrix under different kinds of static loading. Compos Sci Technol 2001;61(11):1615–24.
[29] Ismail Y, Wan L, Chen J, Ye J, Yang D. An ABAQUS® plug-in for generating virtual data required for inverse analysis of unidirectional composites using artificial neural networks. Eng Comput 2022;1–13.
[30] Koerber H, Kuhn P, Ploeckl M, Otero F, Gerbaud P-W, Rolfes R, Camanho PP. Experimental characterization and constitutive modeling of the non-linear stress–strain behavior of unidirectional carbon–epoxy under high strain rate loading. Adv Model Simul Eng Sci 2018;5:1–24.
[31] Camanho PP, Maimí P, Dávila C. Prediction of size effects in notched laminates using continuum damage mechanics. Compos Sci Technol 2007;67(13):2715–27.
[32] Tan W, Naya F, Yang L, Chang T, Falzon B, Zhan L, Molina-Aldareguía J, González C, Llorca J. The role of interfacial properties on the intralaminar and interlaminar damage behaviour of unidirectional composite laminates: Experimental characterization and multiscale modelling. Compos B: Eng 2018;138:206–21.
[33] Allott NR, Czabaj MW. Characterization of the interlaminar shear strength of IM7/8552 using small-scale short beam shear tests. Compos A: Appl Sci Manuf 2021;142:106200.
[34] Soden P, Hinton M, Kaddour A. Biaxial test results for strength and deformation of a range of E-glass and carbon fibre reinforced composite laminates: failure exercise benchmark data. In: Failure criteria in fibre-reinforced-polymer composites. Elsevier; 2004, p. 52–96.